REPORT DOCUMENTATION PAGE

The public reporting burden for this collection of information is estimated to average 1 hour per response, including the time for reviewing instructions, searching existing data sources, gathering and maintaining the data needed, and completing and reviewing the collection of information. Send comments regarding this burden estimate or any other aspect of this collection of information, including suggestions for reducing the burden, to the Department of Defense, Executive Service Directorate (0704-0188). Respondents should be aware that notwithstanding any other provision of law, no person shall be subject to any penalty for failing to comply with a collection of information if it does not display a currently valid OMB control number.
PLEASE DO NOT RETURN YOUR FORM TO THE ABOVE ORGANIZATION.

1. REPORT DATE (DD-MM-YYYY) 09/02/2009	2. REPORT TYPE Final Report	3. DATES COVERED (From - To) October 2005-September 2008

4. TITLE AND SUBTITLE	5a. CONTRACT NUMBER
Life Prediction of High Temperature Polymer Matrix Composites for Aircraft Engine and Airframe Applications	
	5b. GRANT NUMBER FA955-05-1-0481
	5c. PROGRAM ELEMENT NUMBER

6. AUTHOR(S)	5d. PROJECT NUMBER
Roy, Samit* and Lu, Hongbing**	
	5e. TASK NUMBER
	5f. WORK UNIT NUMBER

7. PERFORMING ORGANIZATION NAME(S) AND ADDRESS(ES)	8. PERFORMING ORGANIZATION REPORT NUMBER
* Department of Aerospace Engineering and Mechanics, Box 870280 University of Alabama, Tuscaloosa, AL 35487-0280 **Mechanical and Aerospace Engineering, Oklahoma State University, Stillwater, OK 74083	

9. SPONSORING/MONITORING AGENCY NAME(S) AND ADDRESS(ES)	10. SPONSOR/MONITOR'S ACRONYM(S)
The Mechanics Of Multifunctional Materials & Microsystems Program Air Force Office of Scientific Research 875 N. Randolph Street, AFOSR/NA, Suite 325, Room 3112, Arlington, VA 22203	AFOSR
	11. SPONSOR/MONITOR'S REPORT NUMBER(S) N/A

12. DISTRIBUTION/AVAILABILITY STATEMENT
Unrestricted

13. SUPPLEMENTARY NOTES

14. ABSTRACT
Dynamic experiments were conducted to evaluate the effects of oxidation on the mechanical properties of both 5250-4 resin and its composite under high strain rates. A long split Hopkinson pressure bar was used in experiments. For the resin oxidized at 245 °C for 1500 hrs its mechanical properties, such as Young's modulus and compressive strength, show only slight reduction at high strain rates. For composites oxidized at 195 °C for 1500 hrs, near the service temperature, the changes of mechanical properties are negligible. For composites oxidized at 245 °C for 1500 hrs, when loaded along the fiber direction, the mechanical properties decreases by 1/3, when loaded in other two directions the properties show even more drastic reduction, maintaining only about 1/3 of the stiffness and strength compared with pristine composites. Results indicate that when the composites are subject to a temperature slightly higher than the service temperature, the property degradation is extremely significant. In the modeling task, the micromechanical model was extended to predict progressive failure of a laminate in the presence of nonlinear effects, such as, matrix cracking, fiber/matrix debond, delaminations, and viscoelasticity using fundamental principles of continuum damage mechanics.

15. SUBJECT TERMS
Thermo-oxidation, fiber-matrix debond, diffusion, degradation, progressive failure modeling

16. SECURITY CLASSIFICATION OF:			17. LIMITATION OF ABSTRACT	18. NUMBER OF PAGES	19a. NAME OF RESPONSIBLE PERSON Samit Roy
a. REPORT	b. ABSTRACT	c. THIS PAGE			
U	U	U	SAR	38	19b. TELEPHONE NUMBER (Include area code) 205 348 5883

Standard Form 298 (Rev. 8/98)
Prescribed by ANSI Std. Z39.18
Adobe Professional 7.0

DOD EPSCoR Final Report To The Mechanics Of Multifunctional Materials & Microsystems Program

Project Title: Life Prediction of High Temperature Polymer Matrix Composites for Aircraft Engine and Airframe Applications

Sponsor's Reference Number: FA955-05-1-0481

Program Manager: Dr. Byung L. Lee

Prepared by

Samit Roy* and Hongbing Lu**

* Aerospace Engineering and Mechanics, University of Alabama, Tuscaloosa

** Mechanical and Aerospace Engineering, Oklahoma State University

PART I : MODELING

In this section of the report, oxidation of the polymer in a polymer matrix composite (PMC) used in high temperature applications is modeled using a modified Fick's law of diffusion that includes a reaction term related to the rate of oxygen consumption due to the chemical reaction between the polymer and oxygen. The model incorporates the coupling between oxygen diffusion and polymer consumption process and the resulting shrinkage at the micro-scale. It is conjectured that polymer shrinkage due to thermal oxidation may be responsible for debond to initiate and propagate along fiber-matrix interface, thereby allowing accelerated diffusion and further oxidation. In order to simulate this effect, a cohesive layer model was introduced at the interface of the polymer and fiber within the framework of finite element analysis (FEA) of a micromechanical representative volume element (RVE). Our numerical results indicate that oxygen diffusion at high temperature causes oxidation in the polymer, which indeed leads to thermo-oxidative shrinkage of the polymer that is responsible for the initiation and propagation of fiber/matrix interfacial failure at high temperatures.

The results from the micro-scale FEA/RVE model were subsequently incorporated in a macro-scale laminate model through multi-scale modeling, using continuum damage mechanics. In this report, details of the multi-scale simulation are presented, together with some preliminary experimental data for model verification, in order to gain insight into the anisotropic nature of the thermo-oxidative degradation process and to predict its effect on long-term structural durability.

1.1 INTRODUCTION

The thermal oxidative stability (TOS) of polymer matrix composites for aerospace applications is traditionally determined through long-term aging experiments and extensive test programs. Thermal oxidative aging can result in embrittlement, changes in the glass transition temperature, and micro-cracking ultimately leading to composite stiffness, strength and fracture toughness changes. Various researchers have studied the thermo-oxidative aging process by developing model-based design and novel material systems that enhance the life and affordability of HTPMC.

Colin et al. [1] developed a model based on a differential equation analogous to Fick's law in which the oxygen diffusion and its consumption rate r(C) are coupled, where C is the oxygen concentration. Their model predictions were in excellent agreement with experimental results. More recently, Colin et al. [2] enhanced their kinetic model to predict relative mass loss in a T800H/BMI composite by assuming that the volatile formation results essentially from hydro-peroxide decomposition. The enhanced model was also able to take into account the fact that mass loss is reduced due to the stabilizing effect of carbon fibers due to the scavenging of the peroxyl radicals by carbon. Again, excellent agreement with experimental gravimetric results was observed. Tandon et al. [3, 4] extended the kinetic model by introducing the concept of polymer availability state variable, thereby producing predictive oxidative layer growth simulations for a high temperature polyimide, PMR-15. Macroscopic weight loss measurements were used to determine the reaction and polymer consumption parameters. A parametric sensitivity analysis was used to determine the sensitivity of the controlling parameters. It was observed that the oxidation growth process was diffusion controlled, and that the diffusivity of the oxidized zone is the controlling parameter. Recently, Pochiraju et al. [5] have studied the thermo-oxidative behavior of unidirectional composite material. Their work deals with thermo-

oxidative layer growth and damage growth with time. The modulus of PMR-15 is sensitive to the temperature and oxidation state. Due to strong anisotropy in thermo-oxidative response of G30-500/PMR-15 composite, accelerated oxide layer growth is observed in the fiber direction as compared with the direction transverse to the fibers. Homogenization techniques are used to determine the effective diffusivity of the composite lamina. They have demonstrated the effect of fiber fraction on diffusivity and the effect of a diffusive interface at the lamina scale. It is also observed that compressive modulus of PMR-15 resin decreases from 4.72 to 3.39 GPa due to temperature rise from 25°C to 288 °C as obtained from nano-indentation data of un-oxidized resin. Wang et al [6] have developed a computational micromechanics approach, based on the recently developed coupled constitutive theory with reaction and micro-structural damage is presented for polymer-matrix composites in a high-temperature environment. Micromechanics formulation of the problem is made to include coupled anisotropic thermal oxidation reaction, mass transport, and thermo-mechanical damage in the fiber composites. Numerical solutions are derived for the thermal oxidation problem of a carbon/polyimide composite at elevated temperatures subject to thermo-mechanical loading. Talreja [7] has developed constitutive stress-strain relationships for basic configurations containing distributed damage entities. In this model continuum concept is used which considers composites as homogeneous isotropic body with damage as the internal structure. It uses the basic laws of thermodynamics and damage tensor as internal variables in the functional relationships of response functions. Recently, Talreja [8] discussed multi-scale modeling aspects of damage and operating mechanisms in unidirectional ceramic matrix composites and cross-ply polymer matrix composite laminates. Two multi-scale modeling strategies- continuum damage mechanics and synergistic damage mechanics approach are proposed in the context of deformational response. These are homogenization techniques where material micro-structure and micro-damage structure are treated as smeared tensor fields. A set of response functions are expressed in terms of field variables, which represent the smeared-out fields of evolving damage entities.

This report focuses on developing a micro-mechanics based kinetic approach to determine behavior at macro-scale structural level, though use of continuum mechanics. The strong anisotropy observed in the thermal-oxidation of unidirectional composite lamina is accounted for in this model. Darcy's law is employed to model oxygen permeation in the porous region at the fiber/matrix interface to develop a shrinkage induced, permeation controlled debond growth

model (see Fig. 1). Debond initiation and growth is incorporated in the model through the use of a cohesive layer with a prescribed traction-separation law, and the damage parameters thus obtained are used to predict long-term behavior at the laminate level.

Furthermore, from the experimental data it has been observed that the materials degrades preferentially at the specimen surface perpendicular to the fiber (axial surface), and the rate of oxidation is hastened by micro-cracks opening on the axial surface increasing the surface area for oxidation.

1.2 MATHEMATICAL FORMULATION OF THERMO-OXIDATION MODEL

1.2.1 MODIFIED FICK'S LAW FOR DIFFUSION AND POLYMER CONSUMPTION

Modified Fick's Law for diffusion reaction with orthotropic diffusivity is given by Crank [9],

$$\frac{\partial C}{\partial t} = \left(D_{11} \frac{\partial^2 C}{\partial x^2} + D_{22} \frac{\partial^2 C}{\partial y^2} + D_{33} \frac{\partial^2 C}{\partial z^2} \right) - R(C) \tag{1}$$

with $C(x, y, z, t)$ denoting the oxygen concentration field at time t within a polymer with orthotropic diffusivities D_{ij}, and a polymer consumption reaction rate given by $R(C)$. Three distinct zones – fully oxidized, active reaction, and unoxidized - are typically formed during polymer oxidation [3, 4]. The diffusivity in the active zone is derived based on linear interpolation of the diffusivities in the oxidized and unoxidized regions. The interpolation is carried out using a polymer state variable, ϕ such that $\phi=1$ when the polymer is unoxidized, and $\phi = \phi_{ox}$ when the polymer is fully oxidized. The diffusivity in the active zone is then approximated using he interpolation,

Figure 1. Micrograph of fiber/matrix debond due to thermo-oxidation in G30-500/PMR-15 composite at 288 °C in air. [10]

$$D_{ij}(\phi) = D_{ij}^{un} \frac{\phi - \phi_{ox}}{1 - \phi_{ox}} + D_{ij}^{ox} \frac{1 - \phi}{1 - \phi_{ox}} \tag{2}$$

where, D_{ij}^{un} is the diffusivity in the unoxidized zone and D_{ij}^{ox} is the diffusivity in the oxidized zone.

1.2.2 POLYMER REACTION RATE $R(C)$

The polymer reaction rate is obtained using the mechanistic scheme of branch radical chain reaction developed in [1],

$$R(C) = R_0 f(C) \tag{3}$$

$$f(C) = \frac{2\beta C}{1+\beta C}\left[1 - \frac{\beta C}{2(1+\beta C)}\right] \tag{4}$$

where R_0 is a constant or a temperature dependent parameter and the reaction rate coefficient, β, is a material constant.

1.2.3 EVOLUTION OF POLYMER STATE VARIABLE ϕ

The evolution law for the polymer state variable is given as [3],

$$\frac{d\phi}{dt} = -\alpha R(C) \tag{5}$$

where α is a reaction rate constant. Assuming the initial condition that $\phi = 1$ at $t = 0$ (un-oxidized state) and integrating Equation (5), gives
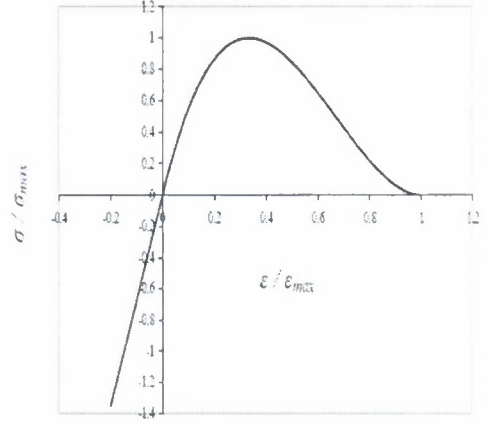
$$\phi(t) = \phi_0 - \int_0^t \alpha R(C)dt = 1 - \int_0^t \alpha R(C)dt \tag{6}$$

If it is assumed that ϕ_{ox} is the cut-off value of ϕ in the oxidized zone when the entire consumable portion of the polymer has been consumed, then $\phi(t) = \phi_{ox}$ in the fully oxidized zone.

5

1.2.4 COHESIVE LAYER MODELING OF ANISOTROPY IN THERMO-OXIDATIVE DEGRADATION

It has been observed in surface weight-loss rate experiments performed on unidirectional G30-500/PMR-15 polymer matrix composite laminate aged at 288°C at Air Force Research Laboratory (AFRL), that oxygen diffusion, and consequently, polymer weight loss exhibits anisotropic behavior. The weight loss in the direction transverse to the fibers is actually lower than the weight-loss for neat resin samples due to the retarding effect of the carbon fibers on oxygen diffusion, as predicated by the rule-of-mixtures. However, the weight loss in the longitudinal (fiber) direction is

Figure 2. Normalized cubic traction-separation law for cohesive layer

observed to be greatly accelerated due to synergistic interactions between the fiber, matrix, and the interface. It is conjectured that polymer shrinkage due to thermal oxidation may be responsible for debond to initiate and propagate along fiber-matrix interface, thereby allowing accelerated penetration of oxygen into the laminate, followed by thermal oxidation. A micrograph showing evidence of fiber/matrix debond due to thermo-oxidative resin shrinkage is presented in Figure 1. In order to simulate this effect, a cohesive layer model was introduced at the interface of the polymer and fiber within the framework of a finite element analysis of a representative volume element (RVE) using an in-house test-bed code (NOVA-3D). Based on a cohesive zone model proposed by Needleman [11], a cubic traction-separation law is employed to simulate the material behavior at the fiber/matrix interface, as shown in Figure 2. In the present model, the cohesive layer is assumed to have a finite thickness, approximately equal to the thickness of the sizing at the fiber/matrix interface. Material properties of the fiber, matrix and cohesive layer are given in Table I. It is important to note that the elastic modulus of polymer matrix varies with ageing time and polymer state variable ϕ as suggested by Wise [12],
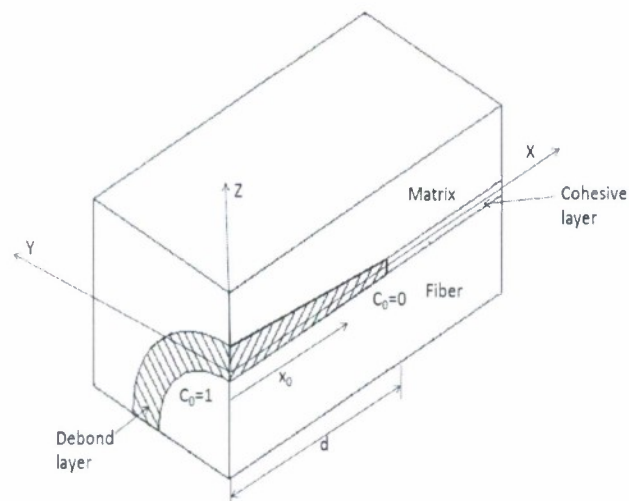
$$E(\phi, T) = E_{un}(T) \exp(K_{ox} \frac{1-\phi}{1-\phi_{ox}}) \exp(K_{nox} \frac{1-\phi}{1-\phi_{ox}} t) \tag{7}$$

where $K_{nox}=0$ and $K_{ox}=0.1878$ for PMR-15. Further, it is notable that significant polymer shrinkage strains - on the order of 30 to 40 % at elevated temperatures - were observed by researchers at the Air Force Research Laboratory (AFRL, Dayton, Ohio).

1.2.5 ANALYTICAL MODEL TO PREDICT DEBOND LENGTH USING DARCY'S LAW FOR OXYGEN DIFFUSION

Figure 3. Debonding due to oxygen permeation/diffusion at the fiber/matrix interface

Assuming that the fiber/matrix debond is initiated and propagated by the shrinkage strain in the surrounding polymer matrix due to oxidative degradation, it is proposed that the debond fracture surface is not smooth, but that it exhibits significant roughness due to the presence of oxidation products as well as fractured polymer fibrils along the interface. Consequently, the flow of oxygen to the debond tip may be represented as axisymmetric flow through a porous media, as depicted in Figure 3. Let x_0 be the debond length (which is assumed equal to length of porous flow regime, assuming flow controlled debond growth), "A" is the pore area of debond, and p is partial pressure of oxygen inside the debond. From Darcy's law of flow in a porous medium, the rate of oxygen flow, u, into the debond region can be written, as given by Williams [13],

$$\frac{dx_0}{dt} = u = \frac{A}{c\eta}\left(\frac{dp}{dx}\right)$$ (8)

Where η is the viscosity and c is a constant. Using Henry's Law, we can define a relation between pressure (p), and concentration of oxygen (C), inside the debond,

Pressure (p) = Concentration (C) × Solubility(S)

Substituting for pressure in equation (8) and assuming solubility is a uniform, the modified form of Darcy's equation in terms of oxygen concentration (C) becomes,

$$\frac{dx_0}{dt} = u = \frac{SA}{c\eta}\left(\frac{dC}{dx}\right)$$ (9)

In the interest of tractability, assuming that oxygen diffusion inside the porous debond is incompressible, the continuity condition can be written as,

$$\frac{du}{dx} + \frac{dv}{dy} = 0$$ (10)

where u and v represent velocity of oxygen flow in the x and y directions, respectively.

For a steady rate of diffusion in transverse direction, $\frac{dv}{dy} = 0$ which gives,

$$\frac{du}{dx} = 0$$

Substituting this result in equation (9) gives,

$$\frac{d^2C}{dx^2} = 0$$ (11)

Or, $\qquad\qquad C = mx + b$

The concentration boundary conditions are,

At x=0 $\qquad\qquad C = C_0$ (oxygen concentration at the free edge)

Or, $\qquad\qquad b = C_0$

At $x=x_0$, $C = 0$ assuming zero oxygen concentration at the debond tip where void nucleation is taking place, giving,

$$m = \frac{-C_0}{x_0}$$

Therefore, $$C = C_0(1 - \frac{x}{x_0})$$ (12)

Combining (9) and (12) gives,

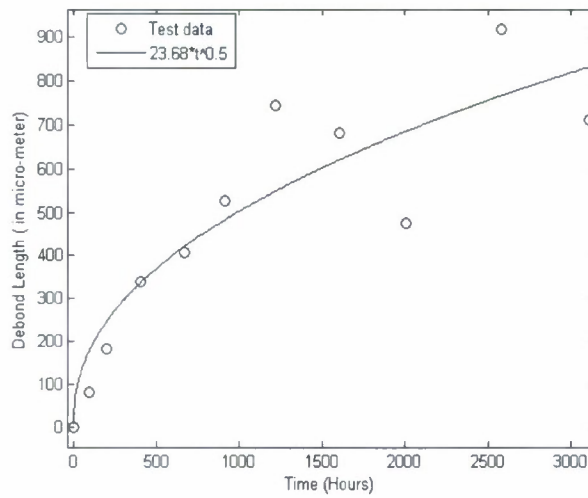$$\frac{dx_0}{dt} = u = \frac{SA}{c\eta}\left(\frac{-C_0}{x_0}\right)$$

Integrating,

$$\int_0^d x_0 dx_0 = -\int_0^t \frac{SA}{c\eta}C_0 dt$$

Or, $$\frac{d^2}{2} = -\frac{SA}{c\eta}C_0 t$$

Or, $$d = \left(\frac{-2SAC_0}{c\eta}\right)^{1/2}\sqrt{t}$$ (13)

where d is the debond length. As evident from equation (13), for permeation controlled debond growth, debond length at the fiber/matrix interface due to oxidative degradation is directly proportional to the square-root of time.

Figure 4. Least squares curve fit for debond length vs. time, of the form $B\sqrt{t}$
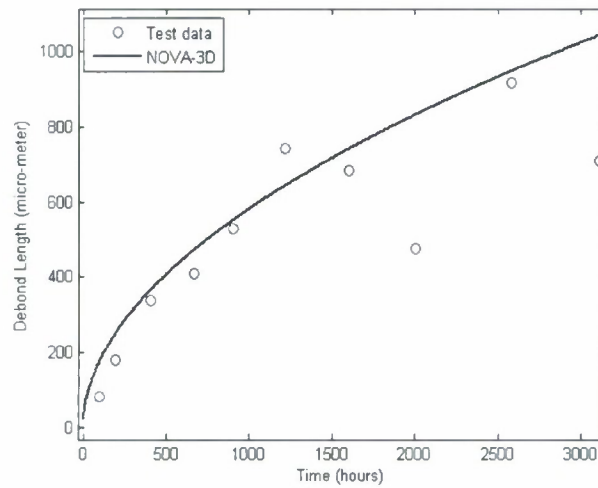
9

Figure 5. Predicted debond length vs. time from FEA analysis (NOVA-3D)
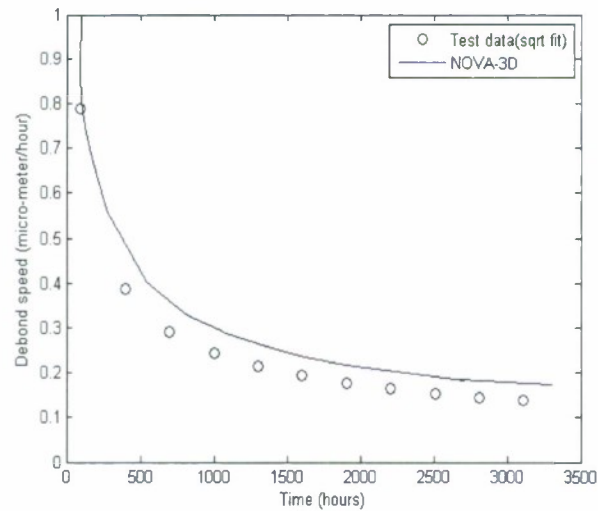

Figure 6. Debond growth rate vs. time using FEA for 5% shrinkage strain.

1.2.6 LEAST-SQUARE FIT FOR DEBOND LENGTH FROM EXPERIMENTS

A least-squares fit was employed to fit the experimental data for debond length due to diffusion complying with square-root of time as shown in Figure 4 for oxidation of a G30-500/PMR-15 unidirectional laminate in air at 288° C. From the least-square fit, the following relationship between debond length d, and time, t was established,

Table 1 : Material properties of G30-500 carbon fiber, polymer matrix (PMR-15) and cohesive layer

Mechanical Properties	Polymer matrix	Carbon fiber	Cohesive layer
Young's modulus (GPa) (un-oxidized)	2.6	240	--
Poisson's ratio	0.36	0.4	--
Maximum stress (MPa)	--	--	10
Maximum strain	--	--	0.1
$D_{un}(\times 10^{-12} m^2 / \min)$	78.6	7.86	78.6
$D_{ox}(\times 10^{-12} m^2 / \min)$	150	15.0	150
$R_0 (\times mol / m^3 . \min)$	0.0583	-	0.0583
Polymer state variable	0.18	-	0.18
Percent Shrinkage Strain	5%	-	5%
α	0.2	-	0.2
β	0.919	-	0.919
λ (CTE) (1/°C)	1.E-5	-	1.E-5
Fiber Radius (R) in (m)	-	2.5×10^{-6}	-

$$d(t) = B\sqrt{t} \qquad (14)$$

where B= 23.68 for G30-500/PMR-15. A comparison of the functional form of equation (14) with equation (13) corroborates the use of Darcy's law for predicting debond length due to permeation controlled debond growth at the micro-scale. Oxygen concentration boundary conditions along the length of the debond given by Equation (12), in conjunction with the diffusion-reaction equation for the polymer matrix (Equation (1)) and cohesive layer element at the fiber/matrix interface were incorporated in a in-house test-bed finite element code (NOVA-3D) to predict debond length as a function of time using a nonlinear finite element solution technique that takes into account the moving boundary at the debond tip. The material parameters used in the simulation are listed in Table 1. Figure 5 shows that the debond length history predicted by NOVA-3D compares well with the evolution of average debond length from experimental data for G30-500/PMR-15, despite some scatter in the test data at higher aging time. In Figure 6, debond growth rate computed from NOVA-3D is compared with least-squares fit of

11

experimental data, again showing excellent agreement. As can be observed from this figure, after debond initiation at fiber/matrix interface near the laminate edge, the initial decrease in debond growth rate is very rapid. Subsequently, the debond growth rate asymptotically approaches a constant value after over 3000 hours of exposure.

1.2.7 ANISTROPIC DAMAGE MODELING FOR FIBER/MATRIX DEBONDING DERIVATION OF DAMAGE MECHANICS MODEL
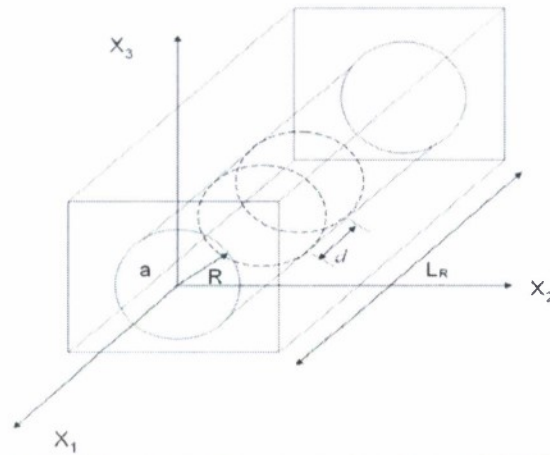

Figure 7. Representative volume element containing fiber/matrix debond.

Based on the continuum damage mechanics (CDM) approach proposed by Talreja [7, 8], Figure 7 shows a representative volume element (RVE) with full circumferential fiber/matrix debond of length d. We assume that the debond surfaces are symmetrical about three orthogonal planes, one of which splits a fiber longitudinally in two halves and the other is normal to the fiber axis. Assuming that the undamaged composite is transversely isotropic with the plane normal to the fiber axis as the plane of isotropy, we define the coordinate axes with X_1 axis parallel to fibers as shown in Figure 7. For an RVE where V_f is fiber volume fraction, R is the fiber radius, L_R is the length of RVE, $d(t)$ is the fiber/matrix debond length in longitudinal direction at time t, and a is a damage influence parameter analogous to mode I crack-opening displacement, a symmetric damage tensor at the debond surface may be defined as [7],

$$d_{ij} = \frac{1}{V_{RVE}} \int_S a n_i n_j dS \tag{15}$$

12

Where, S is the area of the debond surface within the RVE, and the unit normal vector to the debond surface is given by,

$$\bar{n} = \pm \cos\theta\, \hat{e}_2 \pm \sin\theta\, \hat{e}_3 \tag{16}$$

with scalar components $n_1 = 0$, $n_2 = \cos\theta$, and $n_3 = \sin\theta$. The volume of the RVE is given by,

$$V_{RVE} = \frac{\pi R^2 L_R}{V_f} \tag{17}$$

Because the component of the unit normal in the longitudinal direction is zero ($n_1 = 0$) at the debond surface, therefore the component of the damage tensor in the longitudinal (fiber) direction is also zero, i.e. $d_{11} = 0$.

By substituting equations (16) and (17) in equation (15), the components of the damage tensor normal to the debond surface in the X_2-direction at time t, is given by,

$$d_{22}(t) = \frac{1}{V_{RVE}}\left(2\int_0^\pi a\mathrm{Cos}^2\theta.d(t).R.d\theta \right)$$

or, $\qquad d_{22}(t) = \frac{aV_f d(t)}{RL_R} = \delta(t) \tag{18}$

Similarly, it can be shown that the component of the damage in the X_3-direction at time t is,

$$d_{33}(t) = \frac{1}{V_{RVE}}\left(2\int_0^\pi a\mathrm{Sin}^2\theta.d(t).R.d\theta \right) = \frac{aV_f d(t)}{RL_R} \tag{19}$$

It is evident from equations (18) and (19) that $d_{22} = d_{33} = \delta(t)$ and that d_{22} and d_{33} represent same damage entity for a full circumferentially debonded fiber. If the crack opening displacement **a** is assumed to be proportional to a characteristic crack dimension [7], i.e., $a = k\sqrt{S}$, where S is the surface area of the debond, and k is a proportionality constant, then the damage parameter can be written as,

$$\delta(t) = \frac{kV_f d(t)\sqrt{S(t)}}{RL_R} \tag{20}$$

Defining $S(t) = 2\pi Rd(t)$ as the area of debond at time t, the damage parameter can be expressed as,

$$\delta(t) = kV_f \sqrt{2\pi\left(\frac{L_R}{R}\right)}\left(\frac{d(t)}{L_R}\right)^{3/2} \tag{21}$$

1.2.8 FORMULATION OF STIFFNESS COEFFICIENT MATRIX FOR FIBER/MATRIX DEBOND

Thermo-mechanical response of a structure with internal damage can be described using fundamental principles of irreversible thermodynamics [15]. The internal variable for the debond damage configuration is $\delta(t)$ as given by equation (21), and the response function has following form,

$$\Phi = \Phi\ (\varepsilon_{ij},\ \delta) \tag{22}$$

The elements of integrity basis for transversely isotropic symmetry [16], retaining up to second-order term in ε_{ij} and linear terms in δ, assuming $\delta \ll 1$, are,

$$\varepsilon_{11},\ \varepsilon_{22} + \varepsilon_{33},\ (\varepsilon_{22}\text{-}\varepsilon_{33})^2 + 4\varepsilon_{23}{}^2,\ \varepsilon_{12}{}^2 + \varepsilon_{13}{}^2,\ \delta,\ \delta(\varepsilon_{22}\text{-}\varepsilon_{33}),\ \delta\varepsilon_{23},\ \delta\varepsilon_{12}\varepsilon_{13},\ \delta(\varepsilon_{12}{}^2\text{-}\varepsilon_{13}{}^2) \tag{23}$$

The polynomial expansion of the Helmholtz free energy function, Φ, in the absence of residual stresses, takes the following form [7],

$$\rho\Phi = \rho\Phi_0 + \rho\Phi_d \tag{24}$$

where, ρ is the density of the material, Φ_0 is a homogenously quadratic function of strain (ε_{ij}) representing the undamaged state of the material, and Φ_d is a homogeneously quadratic function of strain and a linear function of the damage parameter δ, incorporating the influence of damage on material stiffness. Constructed using the irreducible integrity bases given in equation (23), Φ_d has the following form [7],

$$\begin{aligned}
\rho\Phi_d =&\ A_1\delta\varepsilon_{11}{}^2 + A_2\delta\ (\varepsilon_{22}+\varepsilon_{33})^2 + A_3\delta\varepsilon_{11}(\varepsilon_{22}+\varepsilon_{33}) + A_4\delta[(\varepsilon_{22}\text{-}\varepsilon_{33})^2 + 4\varepsilon_{23}{}^2] + \\
&\ A_5\delta(\varepsilon_{12}{}^2+\varepsilon_{13}{}^2) + A_6\delta(\varepsilon_{12}{}^2\text{-}\varepsilon_{13}{}^2) + A_7\delta\varepsilon_{12}\varepsilon_{13} + A_8\delta\varepsilon_{11}\varepsilon_{23} + A_9\ \delta\ \varepsilon_{23}\ (\varepsilon_{22}+\varepsilon_{33}) \\
&\ + A_{10}\delta\varepsilon_{11}(\varepsilon_{22}\text{-}\varepsilon_{33}) + A_{11}\delta\ (\varepsilon_{22}{}^2\text{-}\varepsilon_{33}{}^2)
\end{aligned} \tag{25}$$

Where, A_1 through A_{11} are constant coefficients. The fourth-rank material stiffness tensor is given by the sum of the undamaged and damaged components,

$$C_{ijkl} = C^0{}_{ijkl} + C^d{}_{ijkl} \tag{26}$$

14

Where, $C^0_{ijkl} = \rho \dfrac{\partial^2 \Phi_0}{\partial \varepsilon_{ij} \partial \varepsilon_{kl}}$ and $C^d_{ijkl} = \rho \dfrac{\partial^2 \Phi_d}{\partial \varepsilon_{ij} \partial \varepsilon_{kl}}$ (27)

Here, C^0 is the stiffness tensor for an undamaged orthotropic elastic material, and the tensor C^d represents the change in stiffness coefficients due to the presence of damage in the form of fiber/matrix debonding.

1.2.9 ENGINEERING MODULI

Linearization of equation (27) leads to expressions for the in-plane engineering moduli after thermo-oxidative damage has taken place, given by [7],

$$E_1^*(t) = E_1^0 + 2\delta(t)[\overline{A}_1 - \overline{A}_2 \nu_{12}^0 + \overline{A}_3 (\nu_{12}^0)^2]$$
$$E_2^*(t) = E_2^0 + 2\delta(t)[\overline{A}_3 - \overline{A}_2 \nu_{21}^0 + \overline{A}_1 (\nu_{21}^0)^2]$$
$$\nu_{12}^*(t) = \nu_{12}^0 + 2\delta(t)\frac{1 - \nu_{12}^0 \nu_{21}^0}{E_2^0}[\frac{1}{2}\overline{A}_2 - \overline{A}_3 \nu_{12}^0]$$
$$G_{12}^*(t) = G_{12}^0 + 2\delta(t)\overline{A}_4 / 4$$

(28)

Where, E_1^0, E_2^0, ν_{12}^0 and G_{12}^0 are the in-plane elastic properties of the undamaged composite lamina, and $\overline{A}_1$, $\overline{A}_2$, $\overline{A}_3$ and $\overline{A}_4$ are constant coefficients from the continuum damage mechanics model. A numerical methodology for determining the unknown coefficients is presented in next section.

1.2.10 EVALUATION OF CONTINUUM DAMAGE MECHANICS COEFFICIENTS

Three-dimensional finite element simulations [17] with cohesive layer at fiber/matrix interface were employed to obtain the damage mechanics coefficients defined in the previous section. The following load cases were simulated applying iso-strain boundary conditions to the RVE depicted in Figure 7:

1. Axial tension (applied normal strain $\varepsilon_{11} = const.$, $\varepsilon_{22}=0$, $\varepsilon_{33}=0$)

2. Transverse tension (applied normal strain $\varepsilon_{22} = const.$, $\varepsilon_{11}=0$, $\varepsilon_{33}=0$)

3. Transverse tension (applied normal strain $\varepsilon_{33} = const.$, $\varepsilon_{11}=0$, $\varepsilon_{22}=0$)

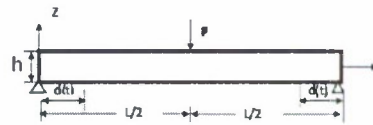4. In-plane-shear (applied shear strain $\gamma_{12} = const.$)

15

The FEA simulations were post-processed to obtain the total strain-energy for the RVE for each of the above reference cases, for a specified debond length, δ. Using energy equivalence between the micromechanical RVE and a smeared orthotropic continuum model of the RVE, the unknown continuum damage mechanics (CDM) coefficients $\overline{A}_1$, $\overline{A}_2$, $\overline{A}_3$ and $\overline{A}_4$ were obtained by employing a least-squares fit. The fiber and matrix properties for G30-500/PMR-15 composite used in these simulations are given in Table I. The CDM coefficients thus obtained are tabulated in Table II. Having determined the CDM coefficients, the orthotropic lamina properties E_1, E_2, ν_{12}, and G_{12}, were then obtained as a function of debond length as defined in Equation (28). The fiber volume fraction for the FEA simulation was assumed to be 0.6.

Table II. Coefficients of CDM for $V_f = 0.6$ (volume fraction of fiber)

CDM coefficients	Values (MPa)
A_1	-3.981×10^3
A_3'	-10.424×10^3
A	-1.513×10^3
A_5'	-1.67×10^3
K	0.02 - 0.05

1.2.11 DAMAGE EVOLUTION MODEL FOR A COMPOSITE LAMINATE

Consider a unidirectional G30-500/PMR-15 laminate of thickness **h** subjected to a load P at the mid-span as shown in Figure 8. In this case study, the unidirectional fibers are assumed to run parallel to the X-axis, and thermo-oxidative degradation of the laminate is assumed to occur primarily due to the progressive debonding of the fiber/matrix interface at the free edges of the laminate induced by shrinkage

Figure 8. Symmetric laminate damage model for three point bending

stresses in the matrix due to oxidation. Assume that the average extent of the zone of thermal-oxidative degradation from the laminate edge is given by d(t), as shown in Figure 8. For an orthotropic unidirectional symmetric laminate undergoing cylindrical bending, the moment curvature relationship reduces to,

16

$$D_{11}^{*} \frac{d^2 w^{*}}{dx^2} = M(x) \qquad\qquad 0<\text{x}<\text{d(t)} \tag{29}$$

Where, the bending stiffness after thermo-oxidative damage,

$$D_{11}^{*} = \frac{1}{12} bh^3 \left(\frac{E_1^{*}}{1 - v_{12}^{*} v_{21}^{*}} \right) \tag{30}$$

In equation (30), **b** is the width of the laminate, and **h** is the thickness, and M(x) is the applied bending moment. Superscript (*) denotes material properties that has undergone thermo-oxidative damage, as defined in equation (28). Assuming that the average length of the interfacial debond is **d(t)** at time **t**, and using symmetry, the moment-curvature relationship for the undamaged laminate can be expressed as,

$$D_{11} \frac{d^2 w}{dx^2} = M(x) \qquad\qquad \text{d(t)}<\text{x}<\text{L/2} \tag{31}$$

Where,
$$D_{11} = \frac{1}{12} bh^3 \left(\frac{E_1^{0}}{1 - v_{12}^{0} v_{21}^{0}} \right) \tag{32}$$

For three-point bending of a simply supported laminate as shown in Figure 8, the bending moment is,

$$M(x) = -\frac{P}{2} x \qquad\qquad 0 < \text{x} < \text{L/2} \tag{33}$$

For the debonded portion of the laminate at time t, substituting (33) in (29),

$$D_{11}^{*} \frac{d^2 w^{*}}{dx^2} = -\frac{P}{2} x$$

Enforcing continuity of deflection and slope at the point where the damaged and the undamaged laminate meet, i.e., at x=d(t),

$$w^{*}(d(t)) = w(d(t)) \tag{34}$$

$$\left. \frac{dw^{*}}{dx} \right|_{x=d(t)} = \left. \frac{dw}{dx} \right|_{x=d(t)} \tag{35}$$

An expression for the deflection at the mid-span of the thermo-oxidative aged laminate can be obtained by combining equations (31)-(35),

17

$$w\left(\frac{L}{2}\right)_{aged} = \frac{PL^3}{48D_{11}} - \frac{Pd^3(t)}{6}\left(\frac{1}{D_{11}} - \frac{1}{D_{11}^*}\right) \tag{36}$$

As a baseline for comparison, the deflection at the mid-span of an equivalent un-aged (undamaged) laminate of length L due to three point bending is given by,

$$w\left(\frac{L}{2}\right)_{unaged} = \frac{PL^3}{48D_{11}} \tag{37}$$

It is evident that equation (36) reduces to equation (37) when debond damage length d(t) is zero, in which event $D_{11}^* = D_{11}$.

If we rewrite equation (36) in the form,

$$w\left(\frac{L}{2}\right)_{aged} = \frac{PL^3}{48\overline{D}_{11}}$$

where, $\overline{D}_{11}$ is the overall effective (damaged) laminate bending stiffness, then,

$$\overline{D}_{11}(d(t)) = \frac{PL^3}{48w\left(\dfrac{L}{2}\right)_{aged}} \tag{38}$$

where $w(L/2)$ is given by equation (36).

Finally, the normalized effective bending stiffness for the aged laminate can be obtained, given by,

$$\frac{\overline{D}_{11}}{D_{11}} = \frac{PL^3}{48D_{11}w\left(\dfrac{L}{2}\right)_{aged}} \tag{39}$$

1.2.12 RESULTS AND DISCUSSION

In the laminate analysis results presented in this section, the evolution of the average fiber/matrix debond length, d(t), as a function of time is obtained using equation (14). The corresponding damage parameter $\delta(t)$ for the laminate analysis is defined by setting the debond length equal to the micromechanical RVE length (i.e., d(t)=L_R) in equation (21), representing a fully debonded fiber/matrix interface of length d(t) at time t, giving,

$$\delta(t) = kV_f \sqrt{2\pi \left(\frac{d(t)}{R} \right)} \tag{40}$$

The predicted variation of normalized bending stiffness ($\overline{D}_{11} / D_{11}$) with normalized fiber/matrix debond length for a unidirectional G30-500/PMR-15 laminate is shown in Figure 9 for different values of the damage opening proportionality constant **k** (refer to equation (20)). Figure 10 depicts the predicted variation of normalized bending stiffness ($\overline{D}_{11} / D_{11}$) with time. From these figures it is evident that, initially, the effect of debond growth on bending stiffness is not very significant until the debond length, d(t), from each edge approaches ~15% of the laminate span. Subsequently, a dramatic reduction in the effective bending stiffness is predicted as the debond length increases with time. A parametric sensitivity study of the influence of the damage opening proportionality constant **k** on effective bending stiffness as depicted in Figures 9 and 10 reveals that the effective bending stiffness is quite sensitive to the value **k** for the range of properties selected in the present analysis.
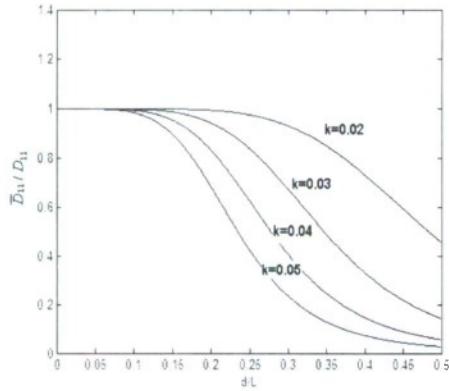
Figure 9. Variation of normalized bending stiffness $\overline{D}_{11} / D_{11}$ with debond length for values of the damage parameter k.
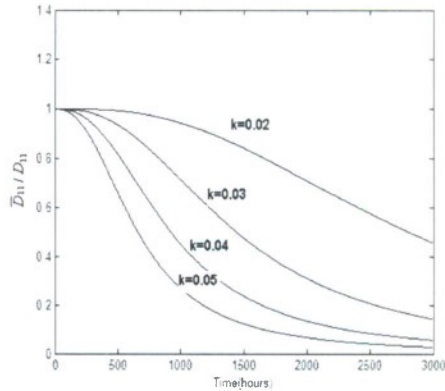
Figure 10. Variation of normalized bending stiffness $\overline{D}_{11} / D_{11}$ with time for different values of the different damage parameter k.

19

PART II: CHARACTERIZATION OF THE VISCOELASTIC BEHAVIOR, THERMAL OXIDATION AND DYNAMIC COMPRESSION OF BMI 5250-4 RESIN AND IM7/5250-4 COMPOSITES

High temperature polymer matrix composites (HTPMC) have been used for structural components in aircraft, including composite frames for turbine engines and engine exhaust washed structures. The service life of HTPMC in numerous situations, however, has been very limited, as low as 100 hours under worst-case operational conditions, due to degradation under harsh environmental conditions primarily due to temperature cycles experienced in flight including both low and high temperatures. Failure of composites in these aggressive environments has a direct impact on operational cost and fleet readiness. In this work we report results on the effects of high temperature on the mechanical behavior of carbon fiber reinforced bismaleimides resin composite CYCOM IM7/5250-4, as well as the matrix material. The matrix material, namely, BMI 5250-4 resin, has a glass transition temperature of 270 °C when it is prepared from the manufacturer specified curing cycle, it has a service temperature up to 204 °C. IM7/5250-4 has been used in primary aircraft structures, including engine nacelles, fuselage skin and stiffeners, wing and stabilizer spars and skins, and other critical load-bearing components, including structures under high temperatures. Both neat resin and composite specimens were thermally oxidized, their shrinkages were measured as a function of time using digital image correlation, and their thermal properties were analyzed using differential scanning calorimetry (DSC). The creep behavior was characterized on both pristine neat resin and thermal oxidized resin; creep master curves were obtained. Nanoindentation measurement was conducted to determine the effects of thermal oxidation on both the oxidized surface layer and cross sectional area of resin specimens under varying oxidation time. A long split Hopkinson pressure bar (SHPB) was used to determine the effects of thermal oxidation on the mechanical properties of both resin and composite at high strain rates.

2.1 CHARACTERIZATION OF QUASI-STATIC TENSILE AND CREEP BEHAVIOR AT SEVERAL TEMPERATURES

Quasi-static tensile testing of ASTM standard dog-bone specimens was conducted on an ATS 2330 arm-level testing machine. Strains on the specimen were measured using high-temperature Epsilon 3555 axial and Epsilon 3675 transverse extensometers. A Load cell installed on the pull rod was used to measure the actual force applied on a specimen. Data was acquired on a Sigma-30 oscilloscope (12-bit resolution) connected with 3603 signal conditioners. Figure 11 shows the Young's modulus and Poisson's ratio as a function of temperature at strain rate $6.1\pm1.5 \times 10^{-4}$ s^{-1}.

Tensile creep testing was conducted at three stress levels, which are ~10%, ~20% and ~30% of the ultimate tensile strength of the resin, 103 MPa as reported by CYCOM. The same dog-bone specimen was tested at room temperature, 64°C, 105°C, 153 °C, 204°C, 263 °C, and 300 °C at each stress level. The specimen was annealed between creep tests to remove the effect of prior loading history. Each tensile creep testing lasted three hours, followed by recovery testing

Figure 11: Young's Modulus and Poisson's Ratio relation with temperature

for one hour. In loading and unloading a ramp loading/unloading was used. The crosshead moves at a speed of 10 mm/min until the set load reached the set values in either loading, or unloading. The loading rate as measured by the load cell in creep testing was approximately 3.1 ± 1.1 MPa/s, and the unloading rate to reach zero stress for recovery testing was 3.2 ± 1.2 MPa /s. The resulting axial strains as a function of time are shown in Figure 12. The corresponding creep compliance functions at these temperatures are shown in Figure 13.

The creep function described by a generalized Kelvin model is given by the following Prony series,

$$J(t) = J_0 + \sum_{i=1}^{N} J_i(1 - e^{-t/\tau_i})$$
(41)

where $J_0, J_1, ..., J_N$ are compliance coefficients, $\tau_1, \tau_2, ..., \tau_N$ are retardation times, and N is a positive integer.
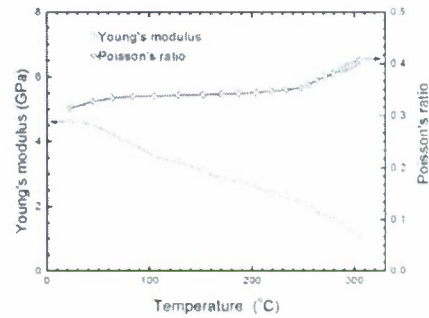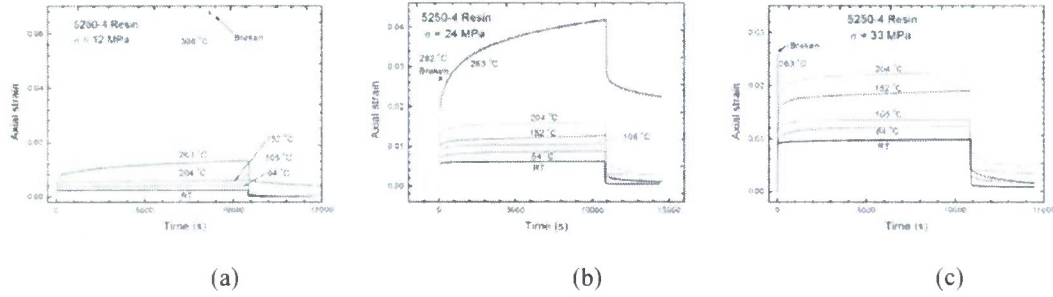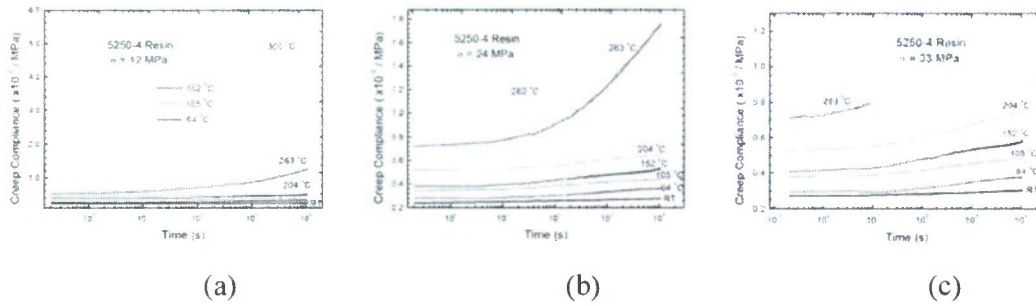
(a)   (b)   (c)
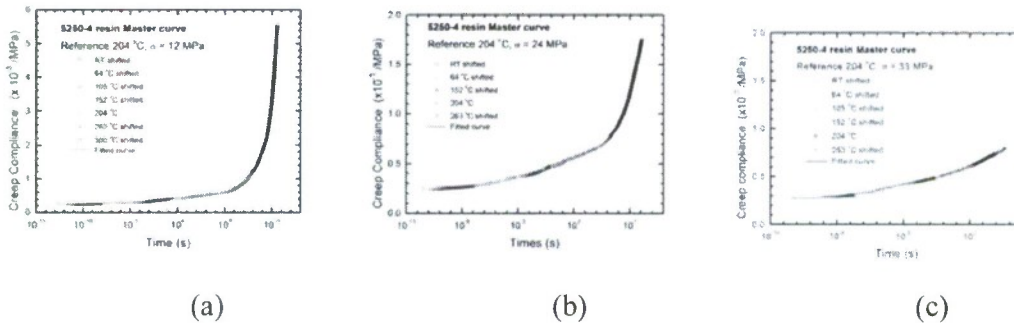
Figure 12: Axial creep strain histories at four temperatures

(a). stress level 12 MPa; (b) stress level 24 MPa; (c) stress level 33 MPa;

(a)   (b)   (c)

Figure 13: Creep compliance at four temperatures

(a). stress level 12 MPa; (b) stress level 24 MPa; (c) stress level 33 MPa;

(a)   (b)   (c)

Figure 14: Master curve at reference temperature 204°C

Using 204 °C as the reference temperature, the creep compliance curves at different temperatures were shifted horizontally to form a smooth master curve at each stress level, as shown in Figure 14. Master curve was fitted into equation (41) to find the best-fit parameters given in Table III. The fitted master curves and shift factors at these three stress levels are shown in Figure 15.

22

(a)   (b)   (c)
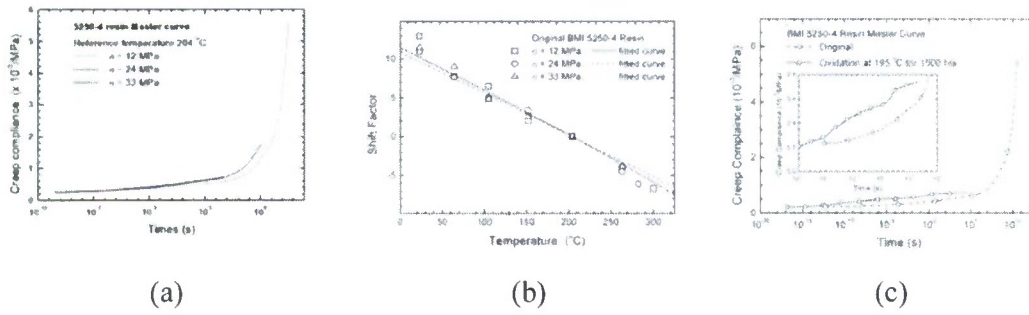
Figure 15: Master curves of BMI 5250-4 resin. (a). at three stress levels;   (b). Shift factors; (c). Comparison
of creep master curves for unoxidized and oxidized resins at 195 °C after 1500 hrs.

For the thermally oxidized resin, resin specimens were placed inside an oven for oxidation in air at 195 °C for two months (~ 1500 hrs). Following the similar procedure used for testing the creep for original resin, creep tests on thermally oxidized resin specimens were conducted under 2.5 MPa at room temperature, 64°C, 153 °C, 185°C, and 202 °C. Each tensile creep testing of oxidized resin lasted 30 hours, followed by recovery for three hours. Using 202 °C as the reference temperature, the creep compliance curves at four temperatures were shifted to form a master curve, as shown in Figure 16. Master curve was fitted into a Prony's series with parameters given in Table III. The Master curves for the original and oxidized resins at 195 °C after 1500 hrs are plotted compared in Figure 15(c). The thermally oxidized resin shows higher creep compliance, indicating that oxidation gives lower stiffness.

(a)   (b)   (c)
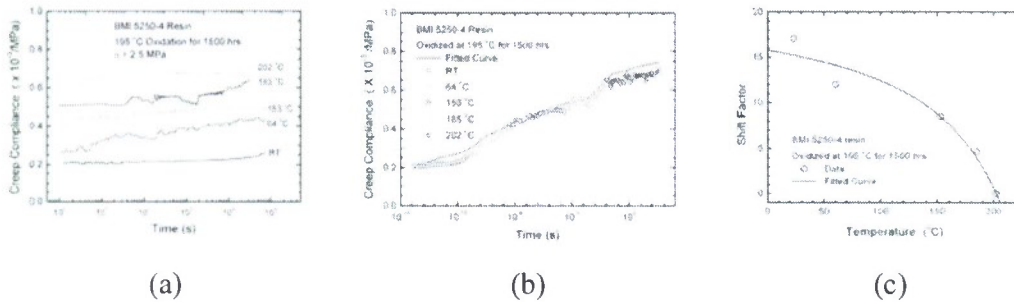
Figure 16: Creep compliances of BMI 5250-4 resin oxidized at 195 °C for 1500 hrs

(a). Creep compliance at different temperatures; (b). Creep master curve; (c) Shift factors

23

**Table III:** Creep Compliance Parameters of 5250-4 Resin

i	τ_i (s)	J_i (10^{-5} /MPa) σ =12 MPa	J_i (10^{-5} /MPa) σ =24 MPa	J_i (10^{-5} /MPa) σ =33 MPa	τ_i (s)	J_i (10^{-5} /MPa) σ = 2.5 MPa
		Original BMI 5250-4 resin			Oxidized resin at 195 °C for 1500 hrs	
1	1×10^{-9}	1.0577	1.3422	1.4882	1×10^{-17}	1.0660
2	1×10^{-8}	1.4869	1.0096	1.0754	1×10^{-16}	1.3499
3	1×10^{-7}	1.1347	1.2243	9.8524	1×10^{-15}	1.8724
4	1×10^{-6}	1.2391	1.1433	1.5339	1×10^{-14}	1.4226
5	1×10^{-5}	1.5110	2.9685	4.6858	1×10^{-13}	1.4167
6	0.0001	1.8483	3.1923	1.9624	1×10^{-12}	2.4696
7	0.001	1.5336	2.6865	2.4335	1×10^{-11}	6.1803
8	0.01	1.7751	1.4557	4.0329	1×10^{-10}	1.6433
9	0.1	4.4153	5.8036	2.3324	1×10^{-9}	4.0269
10	1	1.4305	2.0110	3.2206	1×10^{-8}	2.4841
11	10	5.0852	6.1754	4.4867	1×10^{-7}	1.8696
12	100	3.0229	3.4779	5.4544	1×10^{-6}	2.8719
13	1000	3.8434	5.3998	7.9973	1×10^{-5}	1.1443
14	10000	2.5591	3.6077	4.5293	0.0001	2.5895
15	1×10^{5}	5.9279	11.8377	11.8805	0.001	1.0891
16	1×10^{6}	10.1676	12.4619	67.4551	0.01	9.8710
17	1×10^{7}	17.0269	39.1619	74.4056	0.1	3.6255
18	1×10^{8}	49.0599	62.9005	75.1140	1	9.5886
19	1×10^{9}	37.2922	1.2833	75.1850	10	1.0056
20	1×10^{10}	119.1408	227.1983	75.1921	100	1.7591
21	1×10^{11}	929.3230	268.8350	75.1928	1000	1.7437
22	1×10^{12}	18.8837	273.0266	75.1929	10000	1.0602
23	1×10^{13}	12.3211	273.1561	75.1929	1×10^{5}	1.4466

Residue	1.6564×10^{-8}	2.2263×10^{-9}	6.5387×10^{-9}	Residual	1.4538×10^{-7}
$J_0(10^{-5}/\text{MPa})$	23.7667	24.1795	27.5825	$J_0(10^{-5}/\text{MPa})$	20.40

2.2 NANOINDENTATION MEASUREMENT OF MECHANICAL PROPERTIES OF THERMALLY OXIDIZED 5250-4 RESIN

BMI 5250-4 resin specimens were thermally oxidized and their surface and the cross sectional properties were measured using Berkovich nanoindentation. Before oxidation, the resin samples were washed with soap and rinsed with distilled water for five minutes and then dried with paper towels and placed in a vacuum chamber for at least 48 hrs. During oxidization in oven, the specimens were placed on a fiber glass cloth (initially burned off at 500 °C to remove any possible chemical residues) to prevent direct contact with metal parts of the oven. The oven temperature was controlled at the set temperature (195°C and 280°C, respectively) and the specimens were placed in the oven at different times and then taken out for nanoindentation. A 0.75"×0.75"×0.125" 5250-4 resin plate was placed in an oven at 195 °C for thermal oxidation. The thermally-oxidized resin plate was then removed from the chamber for nanoindetation measurement at room temperature. The specimens used for nanoindentation were stored in a bell jar controlled at a relative humidity of ??% before testing. In all nanoindentation the loading rate used was 0.1 mN/s. Nanoindentation tests were performed at 6~10 different locations on the surface of each resin specimen. The typical load-displacement curves after 3.3 min oxidation are shown 17(a). The curves were reproducible except for the locations where surface was rough. The creep compliance curves, obtained using a method developed specifically for polymers by Lu et al. (2004) are shown in Figure 17 (b) under different thermal oxidation times. The creep compliance at resin surface firstly decreases and then increases with oxidation time. The Young's relaxation modulus calculated from creep compliance data for different thermal oxidation times are shown in Figure 18. The Young's modulus increases and then decreases with oxidation time.

25

(a)   (b)
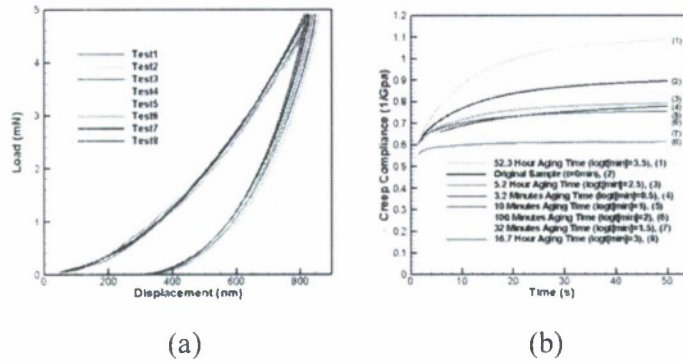
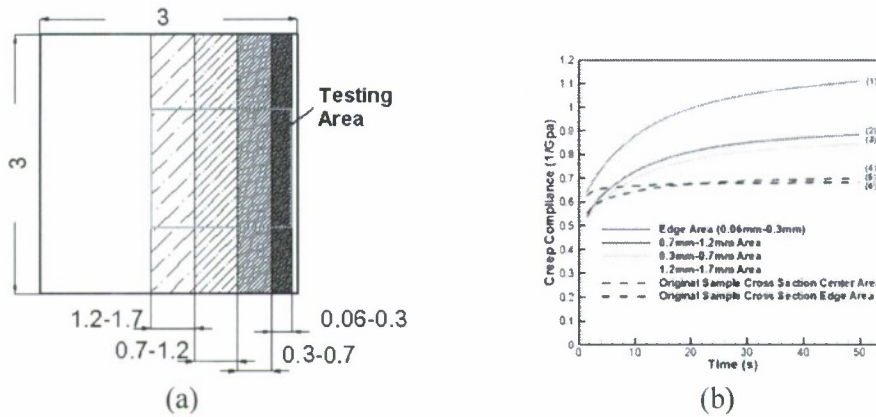**Figure 17:** Nanoindentation results on smooth resin surface after oxidation at 195 °C

(a) Load-displacement curves after 3.2 min oxidation; (b) Creep compliance at different oxidation times.

The effect of oxidation on the surface was also determined from nanoindentation of the cross section using a rectangular specimen of $0.125 \times 0.125 \times 0.3$ in. Using a sharp razor blade, three notched grooves were made on three sides of the cross section ($0.125" \times 0.3"$) with one oxidized side intact initially. Each sample was oxidized at 195 °C in the temperature chamber for 5.2 hours and then taken out for making fresh cross-section surface, obtained by splitting the three grooves using a sharp razor blade to generate smooth surface. Nanoindentation was made starting from the edge of the fractured, un-notched surface to the center (from right to left) following "Testing Areas" marked in Figure 19(a). Nanoindentation tests were conducted at 3~5 different locations along cross-section at each testing area, 0.06~0.3 mm, 0.3~0.7 mm, 0.7~1.2 mm and 1.2~1.7 mm as shown in Figure 19(a). The resulting creep compliance curves at different locations along the cross-section are shown in Figure 19 (b).

From Figure 19 (b), the creep compliance at the edge of cross-section (0.06~0.3 mm) without oxidation is similar to that of the central area (1.5~1.7 mm) after 5.2 hour of oxidation at 204 °C. Except for the first 16 seconds, all creep compliances decrease from the edge area to the center, indicating that the oxidation leads to reduction in stiffness from the resin surface to the central region and form different oxidation layers with varying viscoelastic properties. Resin samples were also oxidized at 280 °C with different oxidation times.
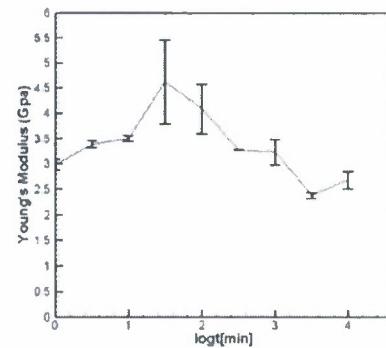
Figure 18: Young's Modulus on smooth resin surface at several oxidation times at 195 °C.

Figure 19: Nanoindentation results of resin on cross-section after 5.2 hour oxidation at 195 °C. (a). Fractured surface with 4 testing areas (units: mm); (b). Creep compliance at different cross-section locations

Typical oxidized resin samples oxidized at 280 °C at several oxidation times are shown in Figure 20. After 523 hours, the resin sample surface starts to warp form bubbles. After 1500 hours, the resin showed debris formed from burning of the resin.

Table IV: Young's relaxation modulus from nanoindentation on cross-section of resin oxidized at 280°C.

	un-oxidized sample modulus (Gpa)	280°C oxidized sample, modulus (GPa)		
		5.2 hrs	52.3 hrs	523 hrs
Edge Area 0-0.3mm	3.92±0.01	2.99±0.06	2.03±0.12	0.12±0.004
0.3mm-0.7mm Area	3.97±0.06	3.24±0.04	2.09±0.12	0.26±0.016
0.7mm-1.2mm Area	3.91±0.04	3.56±0.28	2.85±0.10	1.16±0.013
1.2mm-1.7mm Area	3.72±0.04	3.61±0.05	2.87±0.09	1.86±0.03

The Young's relaxation modulus for resin oxidized for 5.2hrs and 52.3 hrs at 280°C are demonstrated in Figures 21(a)-(d) respectively. The measured Young's relaxation modulus values at time t = 50 s on the cross section at 280°C are presented in Table III.

After oxidized at 280°C for 5.2 hours, the Young's relaxation modulus at edge region decreased about 23.7% while the modulus of the inner core region decreased 3%. For 52.3 hours oxidation, the modulus of resin edge decreased 48% and core modulus decreased 22.8%. After 523 hours oxidation at 280°C, some damages are visible on the sample. The Young's modulus plotted here is the average of multiple measurements. The modulus loss indicates the degradation in resin due to oxidation.
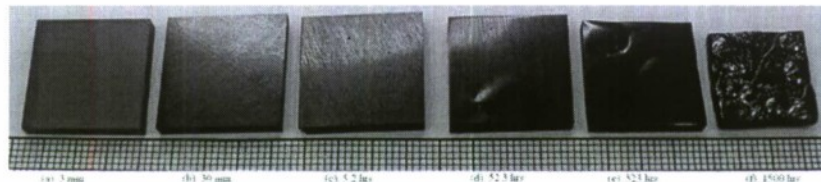

Figure 20. Typical oxidation status of resin at 280 °C with varied oxidized times

2.3 THERMO-OXIDATION SHRINKAGE AND THERMAL ANALYSIS OF 5250-4 RESIN AND COMPOSITES

Two resin samples were used to measure the shrinkage at 260°C oxidation. One was used for observation of the molding surface and the other one was used for observation of the lateral surface, as shown in Figure 22(a), respectively. Through a high-temperature glass window and two light sources illuminating a window, a Nikon D70s camera (12-bit resolution CCD with 3000 × 2000 pixels) was used to acquire images of the resin samples placed inside the oven for oxidation. A speckle pattern was generated using a high-temperature spray paint on the surface
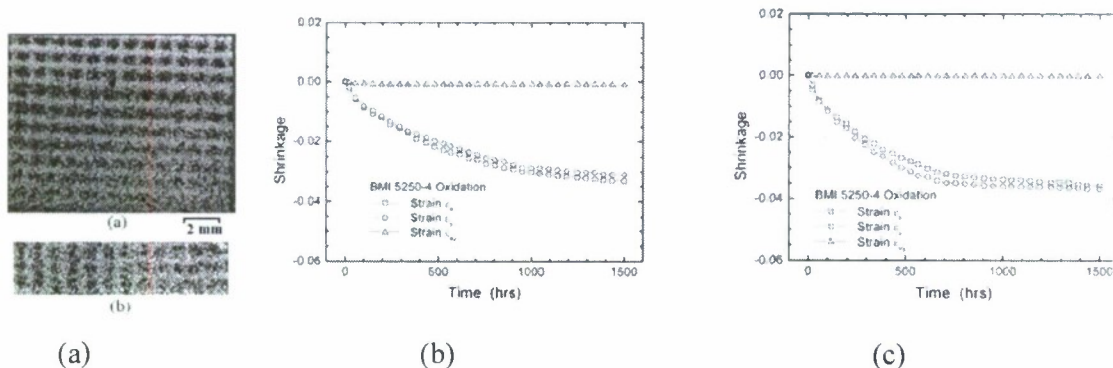

(a)   (b)   (c)

Figure 22: Shrinkage due to oxidation of 5250-4 resin using DIC. (a). Speckle pattern of 5250-4 resin; (b). on the molding surface; (c) on the lateral surface

under observation using black paint dots on while paint background. Digital image correlation (DIC), a non-contact full-field deformation measurement method was used to measure surface strain field on specimens due to oxidation. In DIC, two images, the reference image and the deformed image, are compared to determine the surface deformations through tracking distinct gray scale patterns. The resulting shrinkage strains are shown in Figures 22 (b) and (c). The shrinkage strain is given as the average at each oxidation time. The shrinkage strains are close close for both horizontal and vertical directions showing isotropic shrinkage of resin. The shear strains are negligible.

For IM7/5250-4 composite, we define "x-" direction as fiber direction, "y-" direction as transverse direction, and "z-" the thickness direction as shown in Figures 23 (a) and (b). The composite plates of two thicknesses 0.04" and 0.08" were oxidized at 260 °C with speckle pattern similar to the one on resin, as shown in Figures 23 (c) and (d) , respectively.


(a)   (b)   (c)   (d)
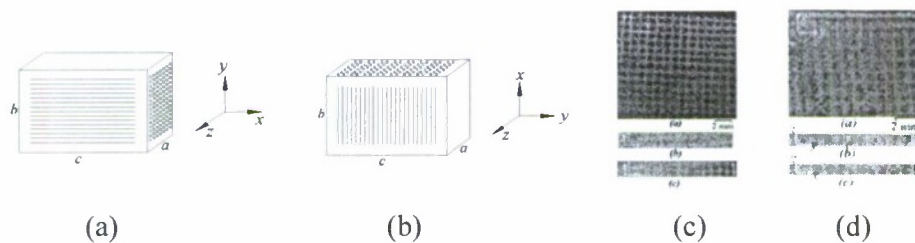
Figure 23: Definition of coordinate system and speckle pattern of composites

[(a). composite with size A; (b). composite with size B; (c). 0.08" thick composite plate; (d). 0.04" thick plate]

For 0.08" thick composite plates, the shrinkage strain in three orientations are shown as in Figure 24. For 0.04" thick composite plates, the shrinkage strain in three orientations are shown as in Figure 25. The thickness effect is significant in oxidation. The shrinkage due to oxidation depends on also the direction with respect to the fiber orientation.

(a)   (b)   (c)
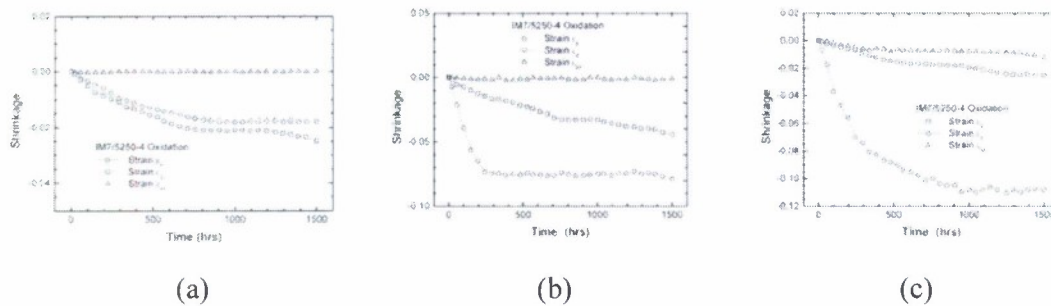
Figure 24: Shrinkage due to Oxidation of 0.08" thick IM7/5250-4 composite determined using DIC.

(a). on the molding surface, z-direction; (b) on cross-section, x-direction; (c) in the lateral direction, y-direction

(a)   (b)   (c)
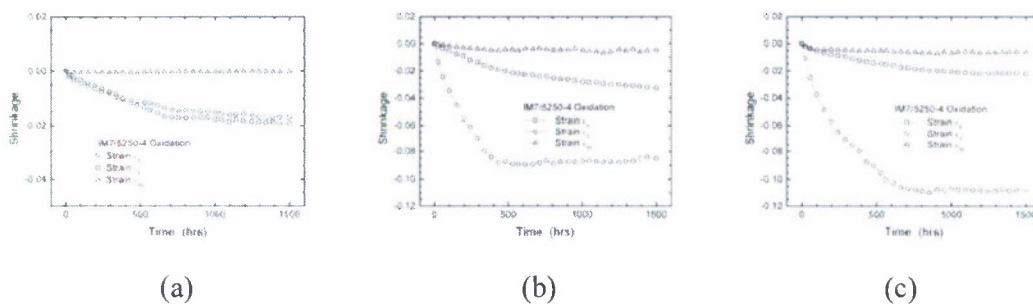
Figure 25: Oxidation shrinkage of 0.04" thick IM7/5250-4 composite using DIC.

(a). in the molding surface, z-direction; (b) in cross-section, x-direction; (c) in the lateral direction, y-direction

(a)   (b)
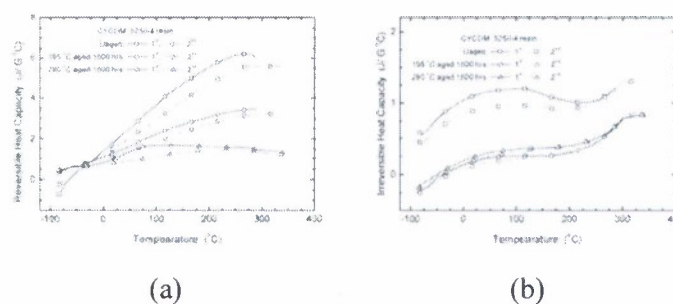
Figure 26: Temperature-modulated DSC heat capacity of oxidized 5250-4 resin.

(a) reversible heat capacity; (b) irreversible heat capacity

The thermal properties were analyzed using differential scanning calorimetry (DSC). In this work we used temperature-modulated differential scanning calorimetry (TMDSC) to determine the heat capacity changes and separate the apparent heat capacity or total heat flow into

30

reversible and irreversible components. A modulated differential scanning calorimeter (TA Instruments Q-1000) using liquid nitrogen for cooling was used to characterize the thermal behavior of un-oxidized and oxidized 5250-4 resins. A sample was cooled to -90 °C and held at this temperature for 5 minutes, then heated at a rate of 10 °C/min with 1 °C/min modulation to a temperature that varied sinusoidally; and the cycle was repeated once for the second run. The reversible and irreversible heat capacities of the pristine and oxidized resins were then determined for the first and the second runs, as shown in Figure 26. For a thermo-set resin, difference between the first and second runs in total heat capacity shows that the BMI resin continues the curing cycle in spite of the oxidation at 195 °C and 280 °C for 1500 hrs. The reversible heat capacity decrease with oxidation temperature, showing reduced heat capability.

2.4 SHPB TESTING OF RESIN AND COMPOSITES BEFORE AND AFTER OXIDATION

Samples of 5250-4 resin and IM7/5250-4 composite were placed inside ovens at 195 °C and 245 °C for oxidation for about 2 months (~1500 hrs). After removal from ovens, the samples were cooled down slowly to room temperature and then stored in a vacuum desicator for at least 72 hrs before SHPB experiments. After 1500 hrs of oxidation, the resin and composites were cut into specimens and used for SHPB testing at high strain rates. The nominal ratio of side lengths of resin and composites a:b:c is 1:2:3. Resin sample is in dimensions of 0.12" ×0.23" in cross-section and 0.34" in length. For composites, the dimensions are 0.08" × 0.24" or 0.08" ×0.17" in cross-section and 0.17" or 0.24" in length, shown as size A and size B in Figures 23 (a) and (b), respectively. The load direction is along the "x-", "y-" or "z-" axis, respectively. An ultra-high-speed camera was employed to acquire images to determine the dynamic deformation for both pristine and oxidized resins. The failed composite samples after SHPB were observed and the oxidized surface was observed under an optical microscope.

(a)   (b)   (c)
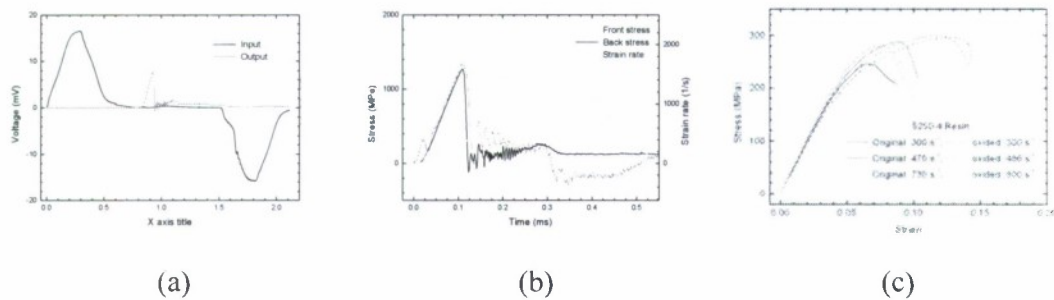
Figure 27: Typical signals and examination of dynamic equilibrium and strain rate for composites and testing results for resins. (a). Typical oscilloscope signals; (b). Dynamic equilibrium examination and strain rate history; (c) Dynamic stress-strain curve of resin.

The typical oscilloscope recording of composite in x-direction was shown in Figure 27(a) and the dynamic equilibrium check indicted a valid testing and strain rate history shows a constant rate in Figure 27(b). All samples were tested 7 or more specimens and the average were reported. The dynamic stress-strain curves of original resin and oxidized resin was shown in Figure 27(c), which indicating that 1500 hrs oxidation at ~245 °C have slightly effect on resin mechanical properties. The stress history associated with the high-speed photography image (Figure 28) shows the un-oxidized Resin failed in axial splitting before the stress peak and oxidized resin failed in axial splitting after the stress peak. Also the failure shows the same mechanism (axial splitting) with different delay failure. Table V summarized the mechanical properties of resin before and after oxidation. Figure 29 show the dynamic stress strain curves of composites in x-, y- and z- direction before oxidation and after two oxidations. Table VI summarized the mechanical properties of composites in three direction loadings before and after oxidation. For 245 °C oxidation after 1500 hrs, the composites shows less properties in x-direction and more weakening (~2/3) than y- and z- direction due that the carbon fiber mainly undertakes the load capability after oxidation. After oxidation, composites in y- direction show more decreased (~1/8) than z-direction (~1/4) properties. The results also show the size effect on SHPB can be ignored with two size composites. Polished z-surface shows slightly higher mechanical properties for original composites while a few for oxidized composites. For 195 °C (slightly less than the service temperature, 204 °C) oxidation after 1500 hrs, the composites shows slightly negligible changes of mechanical properties in x-, y- and z- direction. The molding surface (z-direction) of composites through the curing procedure of the prepreg have

(a)   (b)   (c)   (d)
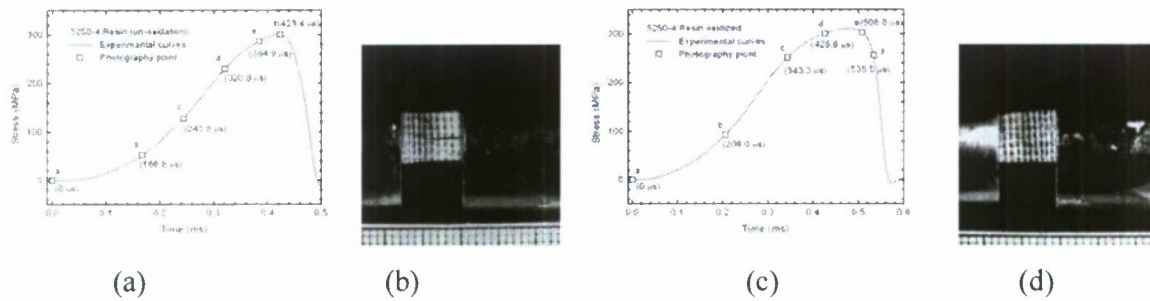
Figure 28: Stress history of resin and failure at begin of axial splitting

(a). original resin; (b). at begin of axial splitting; (c). oxidized resin; (d). at begin of axial splitting;

much surface crack in the resin matrix, as shown in Figure 30 (a). The microscope images of the composite in z-surface before and after 245 °C oxidation, and unpolished and polished surface shows the carbon fiber and de-laminate like crack along the fiber due to oxidation (Figure 30).

**Table V:** SHPB results for 5250-4 resin original and oxidized for 1500 hrs in 245 °C;

5250-4 resin (original)				5250-4 resin (oxidized 1500 hrs in 240~250 °C)			
Strain rate (s^{-1})	Young's modulus (GPa)	Ultimate strength (MPa)	Ultimate strain	Strain rate (s^{-1})	Young's modulus (GPa)	Ultimate strength (MPa)	Ultimate strain
263	4.96±0.07	281±36	9%±2%	286	4.54±0.19	282±44	11%±2%
475	5.02±0.23	298±14	9.8%±1.2%	512	4.65±0.27	289±20	11%±2%
720	5.45±0.20	296±16	10.6%±1.4%	790	5.12±0.10	305±25	14%±4%

(a)   (b)   (c)   (d)
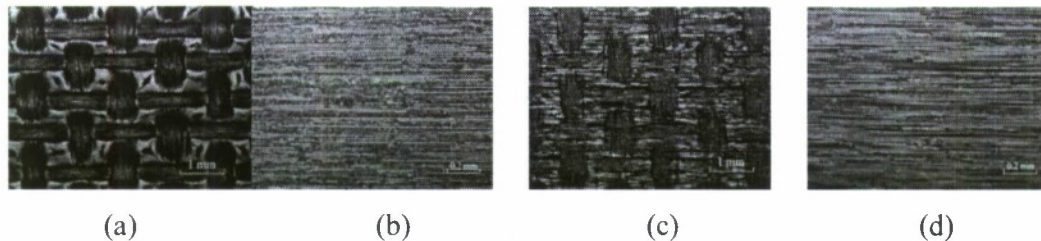
Figure 30: Optical micrographs of composites (in z-surface) before and after 245 °C oxidation

(a). Original surface; (b). Polished original surface; (c). Oxidized surface; (d). Polished oxidized surface;
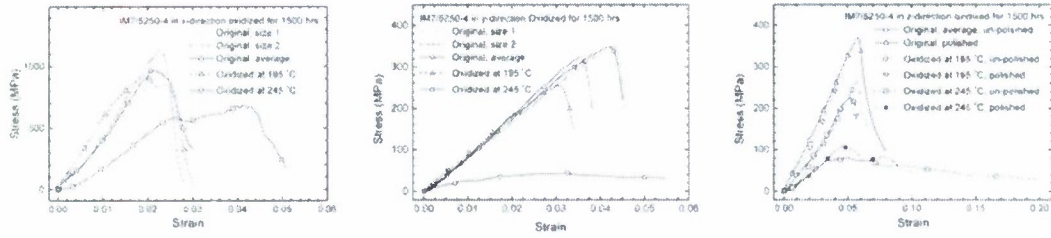
(a). x- direction;   (b). y-direction;   (c). z-direction

Figure 29: Dynamic stress-strain curves of composites at high strain rates

Table VI: Summary of Mechanical Properties of IM7/5250-4 composite before and after oxidation 1500 hrs

Direction	Samples	Ls	Cross-Section	Strain rate (s^{-1})	Young's modulus (GPa)	Ultimate strength (MPa)	Ultimate strain
X-	Original_A	0.245	0.168×0.081	244±135	65.60±15.50	1148±93	2.4±0.8%
	Original_B	0.169	0.242×0.080	239±135	55.81±13.82	1105±119	2.8±0.9%
	Original average	/	/	241±128	60.26±14.76	1124±105	2.6±0.8%
	Oxidized at 195 ºC	0.250	0.180×0.086	237±47	58.50±10.23	967±24	2.0±0.3%
	Oxidized at 245 ºC	0.172	0.217×0.082	334±130	32.98±6.98	758±162	3.2±0.9%
Y-	Original_A	0.168	0.246×0.081	345±251	8.92±0.53	348±22	4.1±0.3%
	Origina_B	0.245	0.169×0.081	333±105	9.53±0.70	312±36	3.4±0.4%
	Original average	/	/	340±189	9.19±0.65	332±33	3.8±0.5%
	Oxidized	0.27	0.170×0.08	387±13	8.60±0.95	277±21	3.6±0.3%

34

	at 195 °C	0	6				
	Oxidized at 245 °C	0.218	0.168×0.081	327±185	3.82±1.14	47±22	1.7±0.4%
Z-	Original	0.081	0.244×0.169	324±90	5.87±0.29	277±21	6.3±0.4%
	Original Polished	0.076	0.246×0.167	216±11	6.45±0.14	389±11	6.2±0.3%
	Oxidized at 195 °C	0.086	0.170×0.270	230±15	5.65±0.12	289±34	4.7±0.1%
	Oxidized at 195 °C Polished	0.076	0.170×0.270	235±15	3,54±0.19	272±10	5.8±0.2%
	Oxidized at 245 °C	0.081	0.219×0.173	300±70	2.67±0.50	110±23	5.0±0.5%
	Oxidized at 245 °C Polished	0.077	0.229×0.171	287±33	2.81±0.48	120±24	4.9±0.3%

CONCLUSIONS

The viscoelastic properties of CYCOM 5250-4 were investigated for high temperature applications. The Young's modulus and Poisson's ratio under the quasi-static tension were also determined as a function of temperature up to 310 °C. Young's modulus decreases from 4.6 GPa at room temperature to 1.05 GPa at 310 °C, and the Poisson's ratio increases from 0.304 at room temperature to 0.407 at 310 °C. The tensile creep behavior of resin was determined at stress levels that are 10%, 20% and 30% of the strength of the resin at their respective testing temperatures. The creep compliance curves at different temperatures were shifted to form a master curve at each of the three stress levels tested. The Prony's series was used to fit the master curve.

Nanoindentation was conducted to measure the mechanical properties at different layers of oxidation. The direct oxidized surface shows that the Young's modulus increases and then decreases with oxidation time. The oxidation in general tends to weaken the mechanical properties, such as Young's modulus. After oxidation at 280°C for 5.2, 52.3 and 523 hours, the Young's relaxation modulus at both edge region and center region decrease. After fully oxidized at 280°C for about 1500 hrs, the resin does not have any load carrying capabilities.

The shrinkage due to oxidation for both resin and composites was determined using the DIC method. The resin shows about 3% shrinkage strain after 1500 hrs oxidation at 260 °C. For the composites the shrinkage depends on the composite thickness and the direction with respect to fiber orientation. The shrinkage strain reached a stabilized value (7%~11%) after about oxidation at 260 °C for 500.

Dynamic experiments were conducted to evaluate the effects of oxidation on the mechanical properties of both resin and composites under high strain rates. A long split Hopkinson pressure bar was used in experiments. For the resin oxidized even at 245 °C for 1500 hrs its mechanical properties, such as Young's modulus and compressive strength, show only slight reduction at high strain rates. For composites oxidized at 195 °C for 1500 hrs, near the service temperature, the changes of mechanical properties are negligible. For composites oxidized at 245 °C for 1500 hrs, when loaded along the fiber direction, the mechanical properties decreases by 1/3, when loaded in other two directions the properties show more drastic reduction, maintaining only about 1/3 of the stiffness and strength compared with pristine composites. Results indicate that when the composites are subject to a temperature higher than the service temperature, the property degradation is extremely significant.

In the modeling task, besides the progress described in this report, work is underway to extend the micromechanical model to predict progressive failure of a laminate in the presence of nonlinear effects, such as, matrix cracking, fiber/matrix debond, delaminations, and viscoelasticity using fundamental principles of continuum damage mechanics (CDM). The viscoelastic compliance master-curves discussed in Part II of this report is being used in the model. A flow chart depicting the primary elements of the proposed multi-scale modeling approach is shown in Figure 31. As can be observed in the flow chart, information from the molecular level modeling (oxygen concentration, polymer consumption rate, etc.) is passed on to a fully three-dimensional micromechanical RVE, where the current state of strain at a given

point in the composite structure is applied on the RVE boundaries to determine failure initiation at the micromechanical
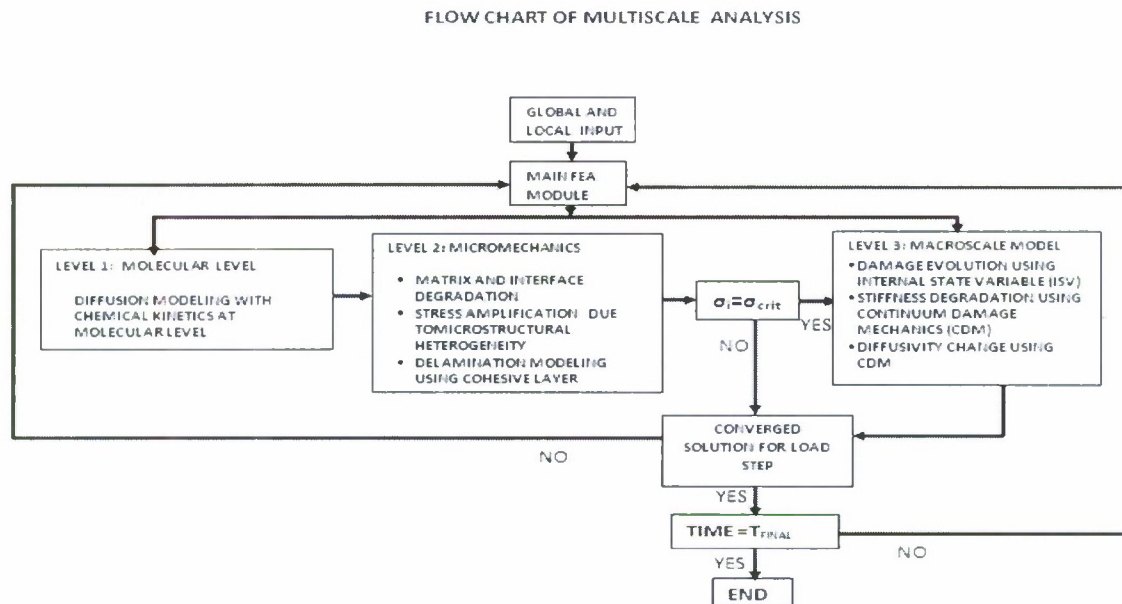
FLOW CHART OF MULTISCALE ANALYSIS

Figure 31: A Flow Chart of Progressive Damage Model

level while fully incorporating stress amplifications due to material heterogeneity. Subsequently, the failure information from the micromechanics level is incorporated in the macro scale structural response through the application of internal state variable within the framework of continuum damage mechanics [8]. Equilibrium iterations are necessary due to the highly nonlinear nature of the problem. The solution process is repeated at each time-step until the maximum allowable structural load/deformation is reached. The progressive failure model was implemented in the in-house finite element code NOVA-3D.

REFERENCES:

1] Colin, X., Verdu, J., 2005. "Strategy for studying thermal oxidation of organic matrix composites" *Composite Science and Technology*, 65, 411-419.

[2] Colin, X., Marais, C., Verdu, J., Jan 2005. "Kinetic modeling of the stabilizing effect of carbon fibers on thermal ageing of thermo-set matrix composites" *Composite Science and Technology*, 65, 117-127.

[3] Tandon, G.P, Pochiraju, K.V, Schoeppner, G.A., 2006. "Modeling of oxidative development in PMR-15 resin" *Polymer Degradation and Stability*.

[4] Pochiraju, K.V., Tandon, *2006. "*Modeling Thermo-Oxidative Layer Growth in High-Temperature Resin", *Journal of Engineering Materials Technology, Vol. 128, pp107-116.*

[5] Pochiraju, K.V., Tandon, G. P., Schoeppner, G.A., *2007. "*Evolution of stress and Deformations in High-temperature Polymer Matrix composites during Thermo-oxidative Aging*", Mechanics of Time Dependent Materials.*

[6] Wang, S. S., Chen, X., 2006. "Computational micro-mechanics for high-temperature constitutive equations of polymer-matrix composites with oxidation reaction", *Journal of Engineering Materials and Technology*, 128, 81-89.

[7] Talreja, R, 1991. "Continuum modeling of damage in ceramic matrix composites", *Mechanics of Material*, 12, 165-180.

[8] Talreja, R, 2006. "Multi-scale modeling in damage mechanics of composite materials" *Journal of Material Science*, 41, 6800-6812, 2006.

[9] Crank, J., 1975. *Mathematics of Diffusion, 2nd Edition, Clarendon Press, Oxford.*

[10] Roy, S., Singh, S., and Schoeppner, G.A., 2007, "Modeling of evolving damage in high temperature polymer matrix composites subjected to thermal oxidation", to appear in a Special Issue of *Journal of Materials Science* on Symposium on Endurance of Composite Materials held at Madeira, Portugal, September 2007.

[11] Needleman, A., 1987. "A continuum model for void nucleation by inclusion debonding", *Journal of Applied Mechanics*, 54, 525-531.

[12] Wise, J., Gillen, K.T. Clough, R.L, 1997. "Quantitative model for the time development of diffusion-limited oxidation profiles" *Polymer*, 38, 1929-1944

[13] Williams, J.G., 1984. *Fracture Mechanics of Polymers, Ellis Horwood Limited.*

[14] Wong, M. S., Skontorp, A., and Wang, S. S., 1994. "Thermal oxidation of carbon fibers and carbon composite at elevated temperature" *Proc. of American Society for Composites 9th Technical Conference*, 458–467.

[15] Coleman, B.D. and Gurtin, M.E., 1967. "Thermodynamics with Internal State Variables", *Journal of Chemical Physics*, 47, 597.